Vibrational and electronic collisional-radiative model in CO2-N2-Ar mixtures for Mars entry problems

Julien Annaloro, Arnaud Bultel

Physics of Plasmas ARTICLE scitation.org/journal/php

Vibrational and electronic collisional-radiative model in CO_2-N_2-Ar mixtures for Mars entry problems

Cite as: Phys. Plasmas **26**, 103505 (2019); doi: 10.1063/1.5114792
Submitted: 11 June 2019 · Accepted: 4 September 2019 ·
Published Online: 11 October 2019

Julien Annaloro[1,2,a)] and Arnaud Bultel[2,b)]

AFFILIATIONS

[1]CNES, 18 Avenue Edouard Belin, 31401 Toulouse Cedex 9, France
[2]CORIA-UMR 6614, Normandie Université, CNRS-Université et INSA de Rouen, Campus Universitaire du Madrillet, 76800 Saint-Etienne du Rouvray Cedex, France

[a)]Electronic mail: Julien.Annaloro@cnes.fr
[b)]Electronic mail: Arnaud.Bultel@coria.fr

ABSTRACT

To predict the nonequilibrium flows around a hypersonic vehicle entering the Martian atmosphere, the two-temperature collisional-radiative model "CoRaM-MARS" has been developed. The species CO_2, CO, C_2, CN, N_2, NO, O_2, C, N, O, Ar, CO^+, C_2^+, CN^+, N_2^+, NO^+, O_2^+, C^+, N^+, O^+, Ar^+, and free electrons are taken into account. The model can therefore be used for conditions belonging to wide ranges of temperatures and pressures. The model is vibrationally specific on the ground electronic state of CO_2, CO, C_2, CN, N_2, NO, and O_2 and electronically specific for all species, with a total of almost 445 vibrational states and 1139 electronic states, respectively. Due to the high temperatures involved (∼40 000 K), a wide set of elementary processes is considered under electron and heavy particle impact reaching $\sim 10^6$ forward and backward elementary processes. The model is implemented in a 1D Eulerian code simulating the shock crossing of the hypersonic flow in the conditions of the entry of the EXOMARS Schiaparelli module into the Martian atmosphere.

I. INTRODUCTION

Since the 1990s, significant works have been devoted to the state-dependent rate coefficient determination. In addition, the computational resources have been substantially improved. It is now possible to elaborate chemical mechanisms at the state level. In the general framework of the next Martian missions dedicated to the ground exploration by probes after a successful landing, the elaboration of a new collisional-radiative (CR) model, able to simulate the complex chemistry of (a) the formation-relaxation of the shock layer in the front of the Thermal Protection System (TPS) of an entering body and (b) the recombination phase close to the after-body, is mandatory to thoroughly estimate the excited state population densities and the resulting radiative fluxes. The present paper aims at presenting this new model called CoRaM-MARS. Its elaboration has been performed similar to our former CoRaM-AIR model.[1] Due to the CO_2-N_2-Ar mixture concerned by the Martian entries, the present model is richer than CoRaM-AIR in terms of excited states. Beyond the vibrational approach used to describe the behavior of the diatomic molecules, one main interest of the present model is the detailed treatment performed for the vibration of CO_2 for which (a) the three modes are separated and (b) the different vibrational excited states are considered as full species and behave freely.

This new model has been implemented in a 1D Eulerian computational fluid dynamics (CFD) code. The relaxation of the mixture is studied in the downstream conditions of a shock produced by the hypersonic entry of the EXOMARS Schiaparelli module into the Martian atmosphere.[2] We assume that the mixture is characterized by two translational temperatures (T_A for heavy particles and T_e for electrons) in thermal nonequilibrium ($T_e \neq T_a$). The electron and heavy particle-induced collisional elementary processes as well as the radiative elementary processes are thoroughly discussed in Sec. II. As far as the missing data are concerned, relevant assumptions are proposed. After the presentation of the database, the specific behaviors of the mixture are analyzed in reference situations. The discussion is focused on the consequences of thermal nonequilibrium on the dissociation-ionization situations. This discussion is provided in Sec. III. The dynamics of the vibrational distributions is analyzed. Those related to the electronic excited states responsible for the radiative signature of

the plasma are also discussed. Finally, we focus our attention on the vibrational distribution of the three modes of CO_2.

II. CoRAM-MARS COLLISIONAL-RADIATIVE MODEL

A. Involved species, database

We have adopted an approach similar to that developed in our model devoted to air.[1] The diatomic molecules have been considered on each vibrational state on their electronic ground state X. However, for CO_2, the situation is more tricky. Indeed, considering CO_2 with the same approach would lead to too many vibrational states owing to the three vibrational modes of this molecule. A rapid estimate has led to about 7500 states assuming a behavior of the harmonic oscillator type and to about 10 000 states assuming that the CO_2 molecules behave like anharmonic oscillators. We have therefore considered a complementary approach for which CO_2 molecules are assumed to be harmonic oscillators and separated in two sets according to their vibrational excitation energy. The first set is denoted as G_1 group molecules whose vibrational energy is lower than a certain threshold $E_v^{G_1\to G_2} = 0.8$ eV. The choice of $E_v^{G_1\to G_2}$ results from the rate coefficients reported in the literature (see Sec. II B 1). In group G_1, the molecules can be simultaneously excited in their different vibrational modes. The related vibrational states are labeled $(v_1\ v_2\ v_3)$ where v_1, v_2, and v_3 are the vibrational quantum numbers relative to the symmetric stretching mode, to the bending mode, and to the asymmetric mode, respectively. The influence of the quantum number l_2 resulting from the vibrational bending[3] has been totally ignored, except for the calculation of the degeneracy of the bending mode excited levels. Beyond the threshold $E_v^{G_1\to G_2}$, the second set G_2 groups the CO_2 molecules that can be considered to be excited in any vibrational mode but with the other modes totally deactivated. The related vibrational states are labeled $(v_1 00)$, $(0 v_2 0)$, or $(00 v_3)$. Using this approach, the global dissociation rate coefficient of CO_2 under self-impact has been estimated and matches rather well the experimental results over the range of $3000\ \text{K} < T_A < 7000\ \text{K}$.[4,5] This approach is more detailed than the one developed by Kozak and Bogaerts[6] but simpler than the one used by Silva *et al.*[7] or Berthelot and Bogaerts[8] since these last authors have also considered the (quadratic) coupling between harmonic oscillators. The model for CO_2 has been finally enriched by the triplet states $^3\Sigma_u^+$, $^3\Delta_u$, $^3\Sigma_u^-$ to have a global view of the electronic excitation of this molecule. The part of the concerned energy diagram is reported in Fig. 1.

The chemistry of the mixture can lead to the formation of numerous compounds. The 21 species concerned CO_2, CO, C_2, CN, N_2, NO, O_2, C, N, O, Ar, CO^+, C_2^+, CN^+, N_2^+, NO^+, O_2^+, C^+, N^+, O^+, and Ar^+ are detailed in Table I. Each vibrational state is considered for the molecules on their electronic ground state. Otherwise, the molecules are treated only on their electronic excitation, as for the atoms and atomic ions. The concerned energy diagram has been taken from the NIST database for the atoms and the atomic ions and from the CoRaM-AIR model for the species N_2, NO, O_2, N_2^+, NO^+, and O_2^+.

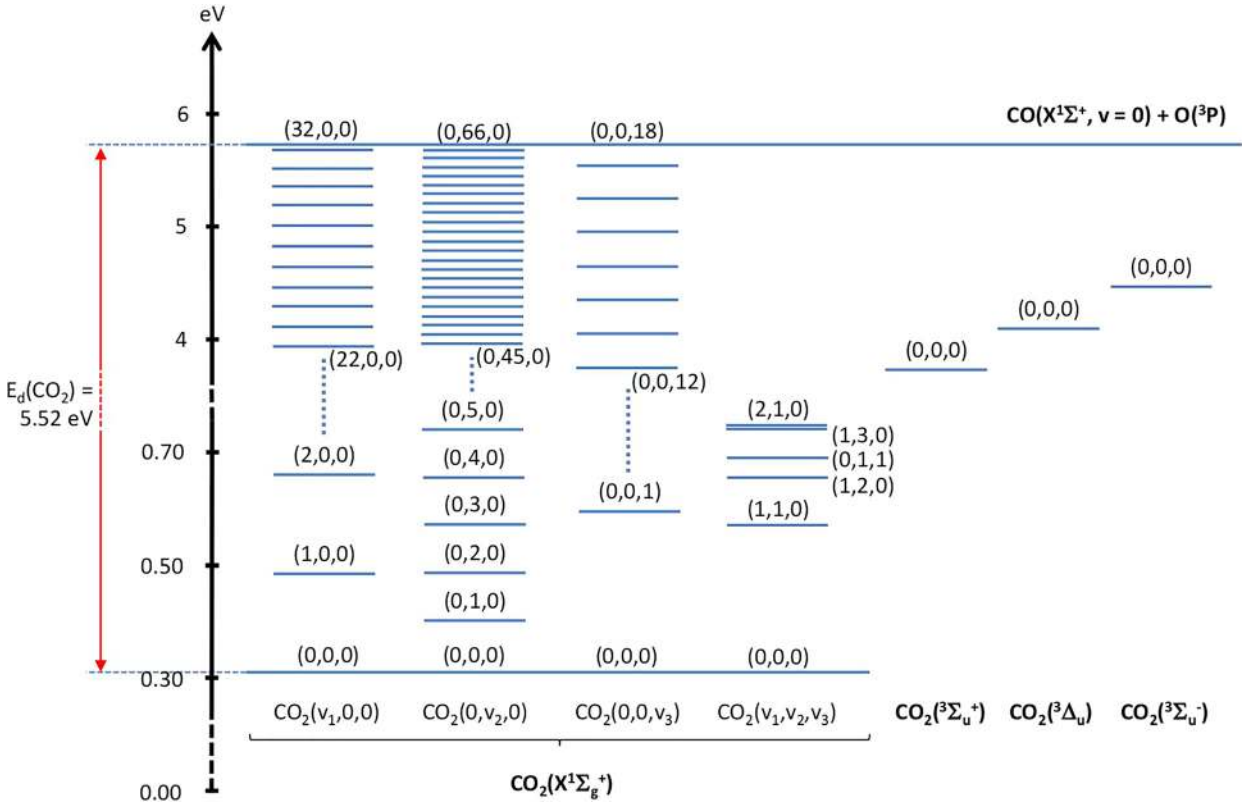

FIG. 1. Energy diagram for the CO_2 molecules.

TABLE I. Species and their different states involved in CoRaM-MARS.

Type	Species	States
Molecules	CO_2	$X^1\Sigma_g^+$ (123 vibrational states), $^3\Sigma_u^+$, $^3\Delta_u$, $^3\Sigma_u^-$
	N_2	$X^1\Sigma_g^+(v=0\rightarrow 67)$, $A^3\Sigma_u^+$, $B^3\Pi_g$, $W^3\Delta_u$, $B'^3\Sigma_u^-$, $a'^1\Sigma_u^-$, $a^1\Pi_g$, $w^1\Delta_u$, $G^3\Delta_g$, $C^3\Pi_u$, $E^3\Sigma_g^+$
	O_2	$X^3\Sigma_g^-(v=0\rightarrow 46)$, $a^1\Delta_g$, $b^1\Sigma_g^+$, $c^1\Sigma_u^-$, $A'^3\Delta_u$, $A^3\Sigma_u^+$, $B^3\Sigma_u^-$, $f^1\Sigma_u^+$
	C_2	$X^1\Sigma_g^+(v=0\rightarrow 36)$, $a^3\Pi_u$, $b^3\Sigma_g^-$, $A^1\Pi_u$, $c^3\Sigma_u^+$, $d^3\Pi_g$, $C^1\Pi_g$, $e^3\Pi_g$, $D^1\Sigma_u^+$
	NO	$X^2\Pi(v=0\rightarrow 53)$, $a^4\Pi$, $A^2\Sigma^+$, $B^2\Pi$, $b^4\Sigma^-$, $C^2\Pi$, $D^2\Sigma^+$, $B'^2\Delta$, $E^2\Sigma^+$, $F^2\Delta$
	CO	$X^1\Sigma^+(v=0\rightarrow 76)$, $a^3\Pi$, $a'^3\Sigma^+$, $d^3\Delta$, $e^3\Sigma^-$, $A^1\Pi$, $I^1\Sigma^-$, $D^1\Delta^-$, $b^3\Sigma^+$, $B^1\Sigma^+$
	CN	$X^2\Sigma^+(v=0\rightarrow 41)$, $A^2\Pi$, $B^2\Sigma^+$, $D^2\Pi$, $E^2\Sigma^+$, $F^2\Delta$
Molecular ions	N_2^+	$X^2\Sigma_g^+$, $A^2\Pi_u$, $B^2\Sigma_u^+$, $a^4\Sigma_u^+$, $D^2\Pi_g$, $C^2\Sigma_u^+$
	O_2^+	$X^2\Pi_g$, $a^4\Pi_u$, $A^2\Pi_u$, $b^4\Sigma_g^-$
	C_2^+	$X^4\Sigma_g^-$, $1^2\Pi_u$, $^4\Pi_u$, $1^2\Sigma_g^+$, $2^2\Pi_u$, $\tilde{B}^4\Sigma_u^-$, $1^2\Sigma_u^+$
	NO^+	$X^1\Sigma^+$, $a^3\Sigma^+$, $b^3\Pi$, $W^3\Delta$, $b'^3\Sigma^-$, $A'^1\Sigma^+$, $W^1\Delta$, $A^1\Pi$
	CO^+	$X^2\Sigma^+$, $A^2\Pi$, $B^2\Sigma^+$, $C^2\Delta$
	CN^+	$X^1\Sigma^+$, $a^3\Pi$, $^1\Delta$, $c^1\Sigma^+$
Atoms	N	$^4S^o_{3/2}$, $^2D^o_{5/2}$, $^2D^o_{3/2}$, $^2P^o_{1/2}$, … (252 states)
	O	$^3P_2$, $^3P_1$, $^3P_0$, $^1D_2$, … (127 states)
	C	$^3P_0$, $^3P_1$, $^3P_2$, $^1D_2$, … (265 states)
	Ar	$^1S_0$, $^2[3/2]^o_2$, $^2[3/2]^o_1$, $^2[1/2]^o_0$, … (379 states)
Atomic ions	N^+	$^3P_0$, $^3P_1$, $^3P_2$, $^1D_2$, … (9 states)
	O^+	$^4S^o_{3/2}$, $^2D^o_{5/2}$, $^2D^o_{3/2}$, $^2P^o_{3/2}$, … (8 states)
	C^+	$^2P^o_{1/2}$, $^2P^o_{3/2}$, $^4P_{1/2}$, $^4P_{3/2}$, … (8 states)
	Ar^+	$^2P^o_{3/2}$, $^2P^o_{1/2}$, $^2S_{1/2}$, $^4D_{7/2}$, … (7 states)

For CO, C_2, CN, CO^+, C_2^+, and CN^+, the energy diagram is derived from the data reported in Refs. 9–19. CoRaM-MARS considers a total of 445 vibrational states and 1139 electronic states.

B. Elementary processes

The mixture is considered to be in thermal nonequilibrium. The electron energy distribution function is assumed Maxwellian at T_e as a result of the efficiency of the elastic collisions. In contrast to the case of discharges,[20,21] no electric field is involved in the present flow conditions and the density is assumed sufficiently high to induce the thermalization of electrons. This assumption avoids the resolution of the Boltzmann equation whose treatment would be time-consuming owing to the high number of states involved. The electron temperature T_e is assumed different from the kinetic temperature T_A. In addition, the rotational mode of the molecules is assumed driven by heavy particle-induced collisions according to time scales shorter than those of the temporal evolutions put forward in Secs. III D and III E. As a result, the rotational distribution is assumed Boltzmannian at T_A. Although previous works[22] have clearly showed that rotation departs from a Boltzmann distribution, this assumption seems justified regarding the calculations performed by Panesi *et al.*[23,24] already discussed for air.[1] The distance required to reach a rotational equilibrium is $x_R = u\,\tau'_R\,n'/n$, where $\tau'_R = 2\times10^{-7}$ s, $n' = 7.2\times10^{22}$ m^{-3}, and n is the density of the present case. We will see in Sec. III D 1 that $u \sim 600$ m s^{-1} and $n \sim 4\times10^{22}$ m^{-3}. This leads to $x_R \sim 2\times10^{-4}$ m and corresponds to positions close to the shock front. Regarding the specific abscissa where dissociation takes place (see Sec. III D 2), the assumption of a Boltzmann distribution for rotation is justified.

All elementary processes taken into account in CoRaM-AIR have been considered in the present model.[1] The related rate coefficients have been reused. In Secs. II B 1–II B 4, we therefore expose the model concerning the additional species only.

1. Vibrational processes and dissociation

We first discuss hereafter the case of CO_2. The model has been elaborated to be used even at low pressure. As a result, the perfect coupling between the first and second vibrational modes of CO_2 through the Fermi resonance

$$CO_2(100) + M \rightarrow CO_2(020) + M \quad (1)$$

may not be systematically observed. We have therefore considered a finite collisional rate for process (1) denoted as k_{FR}. As far as we know, no estimate of this rate coefficient has been experimentally performed at temperature higher than 300 K.[25] We have therefore used the approach described by Herzfeld[26] to obtain the rate coefficient at higher temperature. The results of this approach have been successfully used by Blauer and Nickerson[27] to evaluate numerous rate coefficients involving CO_2 molecules of similar vibrational energy grouped at fictitious levels. The rate coefficient of the Fermi resonance (1) is displayed in Fig. 2. It is important to mention that the rate coefficient weakly depends on T_A. The values are very close to 3×10^{-17} m^3 s^{-1} over the range of 1000 K $< T_A <$ 10 000 K. Joly and Roblin[25] reviewed the experimental values of this rate coefficient, available at 300 K only. The value of 3×10^{-17} m^3 s^{-1} belongs to the experimental interval. As a result, the rate coefficient displayed in Fig. 2 has been used for

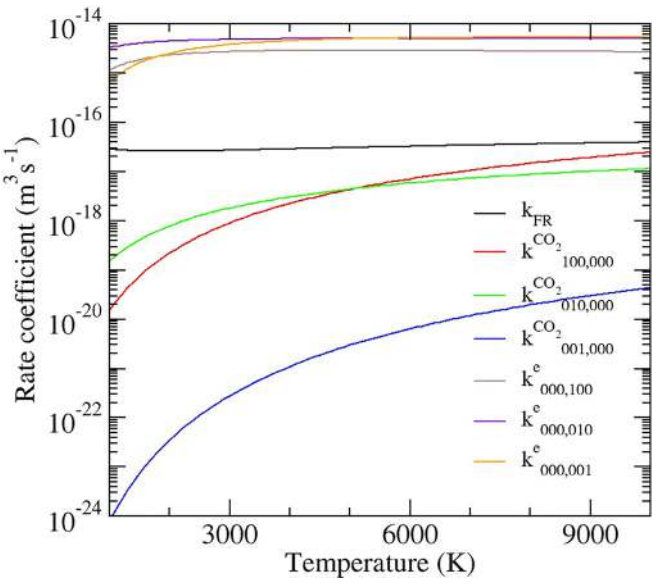

FIG. 2. Temperature dependent rate coefficients k_{FR}, $k^{CO_2}_{100,000}$, $k^{CO_2}_{010,000}$, $k^{CO_2}_{001,000}$, $k^{e}_{000,100}$, $k^{e}_{000,010}$, and $k^{e}_{000,001}$ for the Fermi resonance (1) and the deexcitation processes (2)–(4) and (5)–(7), respectively.

process (1) and for the Fermi resonance arising between molecules if their vibrational energy difference is less than 0.02 eV.

Herzberg's approach has also been used to determine the rate coefficient of the vibration-translation (VT) process under atomic or molecular impact,

$$CO_2(100) + M \rightarrow CO_2(000) + M, \quad (2)$$

$$CO_2(010) + M \rightarrow CO_2(000) + M, \quad (3)$$

$$CO_2(001) + M \rightarrow CO_2(000) + M. \quad (4)$$

The evolution with temperature of the related rate coefficients $k^{M}_{100,000}$, $k^{M}_{010,000}$, and $k^{M}_{001,000}$ is displayed in Fig. 2 for M ≡ CO_2. For the other collision partners, each rate coefficient is multiplied by the collision efficiency η_M with the M-dependent value[27] $\eta_{CO_2} = \eta_O = 1$ and $\eta_{CO} = \eta_{N_2} = \eta_{O_2} = 0.7$. The process has been neglected for the other collision partners. The extrapolation at higher vibrational excitation energy is assumed to be driven by the SSH (Schwartz-Slawsky-Herzfeld) theory.[28] No multiquanta jump has been considered.

For the other VT processes, especially those involving the (v_1 v_2 v_3) levels, rate coefficients have been mainly calculated by Blauer and Nickerson[27] from Herzberg's approach. We have recalculated these rate coefficients since Blauer and Nickerson have considered fictitious levels grouping molecules of similar vibrational energy. This procedure has been also performed for the inter- and intra-vibration-vibration (VV) processes.

The levels of CO_2 molecules can also be populated by the vibration-electron (*Ve*) elementary processes such as

$$CO_2(000) + e^- \rightarrow CO_2(100) + e^-, \quad (5)$$

$$CO_2(000) + e^- \rightarrow CO_2(010) + e^-, \quad (6)$$

$$CO_2(000) + e^- \rightarrow CO_2(001) + e^-. \quad (7)$$

These excitation processes under electron impact have been experimentally studied by several authors whose results have been reviewed by Itikawa.[29] The mean behavior of the cross sections has been considered to derive the rate coefficients $k^{e}_{000,100}$, $k^{e}_{000,010}$, and $k^{e}_{000,001}$ whose temperature dependence is displayed in Fig. 2. The generalization of these processes at higher vibrational excitation has been performed using the procedure recommended by Fridman[30] valid not only for diatomic molecules but also for triatomic molecules. Using this procedure, the rate coefficient for any vibrational excitation $v \rightarrow v'$ under electron impact is proportional to the rate of the $0 \rightarrow 1$ excitation modulated by a relatively simple function of v and v'.

As for diatomic molecules, we have assumed that the dissociation of the CO_2 molecules is the result of the excitation of a virtual vibrational state $v_{max} + 1$ close to the last bound levels ($v_1^{max}00$), ($0v_2^{max}0$), and ($00v_3^{max}$) since T_A is at a maximum value of ∼15 000 K during the dissociation.[31] This excitation may be due to the impact of molecules pumping those of the level v_{max} or to that of atoms pumping molecules of any vibrational level. These assumptions are the same as those considered in CoRaM-AIR, and the rate coefficients considered in Ref. 1 have been reused.

For the CO, CN, and C_2 molecules, vibrational processes have also been taken into account. VT processes under molecular (VT-m) and atomic (VT-a) impact are implemented in CoRaM-MARS. (VV) exchanges can also play a significant role as well as (*Ve*) elementary processes. Table II summarizes these processes. As far as we know, no result has been published on the CO and N_2 vibrational de-excitation under CO_2 and CO molecule impact, respectively. We have therefore assumed that the related rate coefficients are similar to those of the CO vibrational de-excitation under CO impact and the N_2 vibrational de-excitation under N_2 impact reported in Refs. 32 and 33, respectively. These rate coefficients are corrected by the square root of the reduced mass ratio resulting from the fact that the collision partner has changed. It is also important to mention that the elementary data about CN and C_2 are lacking. Analogies are consequently to be done. The spectroscopic constant ω_e of C_2 and CN is close to that of NO and CO, respectively. As a result, the rate coefficients of VT de-excitation $v = 1 \rightarrow 0$ of C_2 and CN have been assumed to be equal to those of the equivalent processes involving NO and CO, respectively. The extrapolation over the vibrational distribution is performed by using a scaling function estimated from the SSH theory, modified for an anharmonic vibrational distribution.[32] For the (*Ve*) processes of C_2 and CN, we have assumed the same $v = 0 \rightarrow 1$ excitation rate coefficient as for NO and for CO, respectively. These $v = 0 \rightarrow 1$ excitation rate coefficients have been calculated by Laporta *et al.*[34,35] The electron energy range concerned by the results displayed in Secs. III D and III E corresponds approximately to the resonance with the associated anion. For N_2, the agreement between the experimental results and those obtained by Laporta *et al.* assuming only the resonant channel are quite satisfactory until electron energies are ∼5 eV.[36] We have therefore neglected the nonresonant channel. The extrapolation over the vibrational distribution is performed using the approach proposed by Fridman.[30]

The rate coefficients for the dissociation of the excited CO, CN, C_2, CO^+, CN^+, and C_2^+ molecules have been taken from the work of Park,[37] Gorelov *et al.*,[38] and Lecointre *et al.*[39] For the dissociation of diatomic molecules not reported in the previous references, we have taken the rate coefficients estimated in our previous work.[1,40]

TABLE II. Vibrational processes implemented in CoRaM-MARS involving CO, CN, and C_2 and additional $N_2(v)$ and $NO(v)$ elementary processes with respect to CoRaM-AIR.[1]

Processes	Reactions	References	Processes	Reactions	References
VT-m	$CO(v) + CO \rightarrow CO(v-1) + CO$	32	VT-a	$CO(v) + O \rightarrow CO(v-1) + O$	32
	$CO(v) + N_2 \rightarrow CO(v-1) + N_2$	75		$C_2(v) + O \rightarrow C_2(v-1) + O$	32[a]
	$CO(v) + CO_2 \rightarrow CO(v-1) + CO_2$	32[b]		$CN(v) + O \rightarrow CN(v-1) + O$	32[c]
	$NO(v) + CO \rightarrow NO(v-1) + CO$	75			
	$N_2(v) + CO \rightarrow N_2(v-1) + CO$	33[b]			
VV	$CO(v) + CO(w-1) \rightarrow CO(v-1) + CO(w)$	32	*Ve*	$CO(v) + e^- \rightarrow CO(w > v) + e^-$	35
	$CO(v) + N_2(w-1) \rightarrow CO(v-1) + N_2(w)$	75		$C_2(v) + e^- \rightarrow C_2(w > v) + e^-$	34[a]
	$NO(v) + CO(w-1) \rightarrow NO(v-1) + CO(w)$	75		$CN(v) + e^- \rightarrow CN(w > v) + e^-$	35[c]

[a]NO analogy based on similar ω_e values.
[b]Reduced mass ratio correction.
[c]CO analogy based on similar ω_e values.

Under heavy particle impact, the dissociation rate coefficient depends on the vibrational excitation of the excited molecule concerned. Since the vibrationally specific approach is used for the ground electronic states only, an assumption is done about the vibrational distribution of the excited electronic states of CO_2, CO, CN, and C_2. We assumed that this distribution is Boltzmannian with the vibrational temperature T_v calculated as the excitation temperature of the first five vibrational states of the ground electronic state of the related molecule. This excitation temperature can be considered as a "vibrational temperature" if the calculated distribution is not too far from a Boltzmann distribution. The dissociation rate coefficient under heavy particle impact is then assumed driven by the correction of Krivonosova *et al.*[41]

The rate coefficients reported by the literature are often related to electronic states without information about the vibrational state dependence. Starting from the rate coefficient k for the whole distribution, we use the Vibrational Reallocation Procedure (VRP) to derive the vibrationally dependent rate coefficient k_v.[1,42]

Regarding the noncarbonated molecules, all the collisional model of Refs. 1 and 42 has been completely reused, including, in particular, the multiquanta transitions.[43–45]

2. Electronic excitation and ionization

a. Molecular species. The ionization rate coefficient under heavy particle impact has been calculated using Eq. (12) of our paper,[1] whereas that under electron impact has been calculated using Eq. (13) of the same paper. The excitation from the ground state $X^1\Sigma_g^+$ has been calculated using Eq. (12) for the heavy particle-induced collisions[1] and Eq. (14) for the electron-induced collisions since the transition is optically forbidden.[1] Some rate coefficients are listed in Table III.

The electronic excitation of N_2, O_2, NO, and N_2^+ under CO impact has been derived from the work of Park.[37] The work of Surzhikov,[46] Zalogin *et al.*,[47] and Park[37] have been used concerning the electronic excitation of CO, CN, and C_2 for a part of the excited states listed in Table I. Again, the lack of data for CN and C_2 has to be underlined. For the other states, the rate coefficient numbered (12) in our paper[1] devoted to air has been used and some of them are reported in Table III.

The same procedure has been performed for processes under electron impact. The work of Riahi *et al.*,[48] Olszewski *et al.*,[49] Brunger and Buckman,[50] Zalogin *et al.*,[47] Park,[51] and Freund *et al.*[52] have been used for CO, CN, C_2^+, and CO. For the rate coefficient relative to excited states not reported in the previous papers, we have used the analytical forms numbered (13) and (14) of our paper[1] devoted to air for allowed and forbidden transitions, respectively.

b. Atomic species. For C and C^+, the formalism due to Drawin[53] has been used since the experimental results are scarce. The relevance of the cross-sectional set proposed by Drawin has been in part validated by the calculation of global ionization and recombination rate coefficients whose values are in relatively good agreement with experimental results.[54]

3. Neutral exchange

The rate coefficient for the carbonated species has been treated in the following way. The rate coefficients of the exchange processes,

$$C_2(d) + O \rightarrow CO(X) + C, \quad (8)$$

$$O_2(X) + C \rightarrow CO(a) + O, \quad (9)$$

are due to Aliat[55] and to the interpolation used in the GriMech 3.0 chemical mechanism[56] over the range of $300\,K < T_A < 3000\,K$, respectively. We have considered that the latter rate coefficient can be used at higher temperature. From these values, those for the processes,

$$C_2(i) + O \rightarrow CO(j) + C, \quad (10)$$

$$O_2(i) + C \rightarrow CO(j) + O, \quad (11)$$

have been determined by using the following assumptions. The elementary rate coefficient presents a modified Arrhenius form of the type $k(T) = A\,T^{\alpha}\,e^{-\Delta E_{XX'}/(k_B T)}$, where $\Delta E_{XX'}$ is equal to the threshold energy if the process is inelastic or is equal to zero elsewhere. The process occurs to satisfy the Wigner and Witmer[57] rule of correlation of spin and orbital momentum between reactive and product species (a factor of 1/10 is then used if this rule is violated).

Other neutral exchange processes have been taken into account. In particular, those producing CO_2 from a collision between CO (in particular, the backward process of the Boudouard process[58]), O_2, and

TABLE III. Parameters A, α, and $B = \Delta E/k_B$ of the rate coefficient written under the modified Arrhenius form $k(T) = A\,T^{\alpha}\,e^{-\Delta E/(k_B T)}$ of some excitation, neutral exchange, and ionization processes under heavy particle impact implemented in CoRaM-MARS.

	Parameters of the rate coefficient $k(T_A) = A\,T_A^{\alpha}\,\exp(-B/T_A)$ expressed in $m^3\,s^{-1}$			
Elementary processes	A ($m^3\,s^{-1}\,K^{-\alpha}$)	α	B (K)	References
$CO_2(X^1\Sigma_g^+) + CO_2(X^1\Sigma_g^+) \rightarrow CO_2(^3\Sigma_u^+) + CO_2(X^1\Sigma_g^+)$	7.443×10^{-26}	1.069	40854	Equation (12) of Ref. 1
$CO_2(X^1\Sigma_g^+) + CO_2(X^1\Sigma_g^+) \rightarrow CO_2(^3\Delta_u) + CO_2(X^1\Sigma_g^+)$	6.995×10^{-26}	1.078	45089	Equation (12) of Ref. 1
$CO_2(X^1\Sigma_g^+) + CO_2(X^1\Sigma_g^+) \rightarrow CO_2(^3\Sigma_u^-) + CO_2(X^1\Sigma_g^+)$	6.467×10^{-26}	1.064	49311	Equation (12) of Ref. 1
$CO_2(^3\Sigma_u^+) + CO_2(X^1\Sigma_g^+) \rightarrow CO_2(^3\Delta_u) + CO_2(X^1\Sigma_g^+)$	1.073×10^{-24}	1.466	2996	Equation (12) of Ref. 1
$CO_2(^3\Sigma_u^+) + CO_2(X^1\Sigma_g^+) \rightarrow CO_2(^3\Sigma_u^-) + CO_2(X^1\Sigma_g^+)$	2.531×10^{-25}	1.408	6800	Equation (12) of Ref. 1
$CO_2(^3\Delta_u) + CO_2(X^1\Sigma_g^+) \rightarrow CO_2(^3\Sigma_u^-) + CO_2(X^1\Sigma_g^+)$	1.067×10^{-24}	1.465	3005	Equation (12) of Ref. 1
$CO_2(i) + CO(X^1\Sigma^+) \rightarrow CO_2(j) + CO(X^1\Sigma^+)$	$k_{CO_2(i)+CO(X^1\Sigma^+)} = 1.134 \times k_{CO_2(i)+CO_2(X^1\Sigma_g^+)}$			
$CO_2(i) + O(^3P) \rightarrow CO_2(j) + O(^3P)$	$k_{CO_2(i)+O(^3P)} = 1.370 \times k_{CO_2(i)+CO_2(X^1\Sigma_g^+)}$			
$CO(X^1\Sigma^+) + CO_2(X^1\Sigma_g^+) \rightarrow CO(I^1\Sigma^-) + CO_2(X^1\Sigma_g^+)$	1.131×10^{-26}	1.097	87895	Equation (12) of Ref. 1
$CO(X^1\Sigma^+) + CO_2(X^1\Sigma_g^+) \rightarrow CO(D^1\Delta^-) + CO_2(X^1\Sigma_g^+)$	1.032×10^{-26}	1.102	88990	Equation (12) of Ref. 1
$CO(X^1\Sigma^+) + CO_2(X^1\Sigma_g^+) \rightarrow CO(a'^3\Sigma^+) + CO_2(X^1\Sigma_g^+)$	2.648×10^{-26}	1.054	75823	Equation (12) of Ref. 1
$CO(X^1\Sigma^+) + CO_2(X^1\Sigma_g^+) \rightarrow CO(d^3\Delta) + CO_2(X^1\Sigma_g^+)$	1.678×10^{-26}	1.075	82791	Equation (12) of Ref. 1
$CO(X^1\Sigma^+) + CO_2(X^1\Sigma_g^+) \rightarrow CO(e^3\Sigma^-) + CO_2(X^1\Sigma_g^+)$	1.235×10^{-26}	1.092	86815	Equation (12) of Ref. 1
$CO(X^1\Sigma^+) + O(^3P) \rightarrow CO(i) + O(^3P)$	$k_{CO(i)+O(^3P)} = 1.297 \times k_{CO(i)+CO_2(X^1\Sigma_g^+)}$			
$CO(X^1\Sigma^+) + CO_2(X^1\Sigma_g^+) \rightarrow CO^+(X^2\Sigma^+) + e^- + CO_2(X^1\Sigma_g^+)$	1.202×10^{-28}	1.817	14479	Equation (12) of Ref. 1
$CN(X^2\Sigma^+) + CO(X^1\Sigma^+) \rightarrow CN(D^2\Pi) + CO(X^1\Sigma^+)$	3.320×10^{-24}	1.050	73953	Equation (12) of Ref. 1
$CN(X^2\Sigma^+) + CO(X^1\Sigma^+) \rightarrow CN(E^2\Sigma^+) + CO(X^1\Sigma^+)$	2.201×10^{-24}	1.067	80608	Equation (12) of Ref. 1
$CN(X^2\Sigma^+) + CO(X^1\Sigma^+) \rightarrow CN(F^2\Delta) + CO(X^1\Sigma^+)$	2.063×10^{-26}	1.070	81556	Equation (12) of Ref. 1
$CN(X^2\Sigma^+) + O(^3P) \rightarrow CN(i) + O(^3P)$	$k_{CN(i)+O(^3P)} = 1.167 \times k_{CN(i)+CO(X^1\Sigma^+)}$			
$C_2(X^1\Sigma_g^+) + CO(X^1\Sigma^+) \rightarrow C_2(a^3\Pi_u) + CO(X^1\Sigma^+)$	1.150×10^{-22}	1.498	488	Equation (12) of Ref. 1
$C_2(X^1\Sigma_g^+) + CO(X^1\Sigma^+) \rightarrow C_2(b^3\Sigma_g^-) + CO(X^1\Sigma^+)$	3.086×10^{-25}	1.403	7136	Equation (12) of Ref. 1
$C_2(X^1\Sigma_g^+) + CO(X^1\Sigma^+) \rightarrow C_2(A^1\Pi_u) + CO(X^1\Sigma^+)$	2.060×10^{-23}	1.364	9885	Equation (12) of Ref. 1
$C_2(X^1\Sigma_g^+) + CO(X^1\Sigma^+) \rightarrow C_2(c^3\Sigma_u^+) + CO(X^1\Sigma^+)$	1.325×10^{-25}	1.276	17056	Equation (12) of Ref. 1
$C_2(X^1\Sigma_g^+) + CO(X^1\Sigma^+) \rightarrow C_2(C^1\Pi_g) + CO(X^1\Sigma^+)$	8.859×10^{-26}	1.072	46841	Equation (12) of Ref. 1
$C_2(X^1\Sigma_g^+) + CO(X^1\Sigma^+) \rightarrow C_2(e^3\Pi_g) + CO(X^1\Sigma^+)$	7.263×10^{-26}	1.049	55493	Equation (12) of Ref. 1
$C_2(X^1\Sigma_g^+) + CO(X^1\Sigma^+) \rightarrow C_2(D^1\Sigma_u^+) + CO(X^1\Sigma^+)$	6.450×10^{-24}	1.044	59371	Equation (12) of Ref. 1
$C_2(X^1\Sigma_g^+) + O(^3P) \rightarrow C_2(i) + O(^3P)$	$k_{C_2(i)+O(^3P)} = 1.161 \times k_{C_2(i)+CO(X^1\Sigma^+)}$			
$C_2(X^1\Sigma_g^+) + O(^3P) \rightarrow CO(X^1\Sigma^+) + C(^3P)$	7.760×10^{-14}	−0.541	0	Equation (12) of Ref. 1
$C_2(X^1\Sigma_g^+) + O(^3P) \rightarrow CO(a^3\Pi) + C(^3P)$	6.272×10^{-14}	−0.541	11936	Equation (12) of Ref. 1
$C_2(X^1\Sigma_g^+) + O(^3P) \rightarrow CO(a'^3\Sigma^+) + C(^3P)$	5.331×10^{-13}	−0.541	21831	Equation (12) of Ref. 1
$C_2(X^1\Sigma_g^+) + O(^3P) \rightarrow CO(d^3\Delta) + C(^3P)$	1.137×10^{-14}	−0.541	29406	Equation (12) of Ref. 1
$C_2(X^1\Sigma_g^+) + O(^3P) \rightarrow CO(e^3\Sigma^-) + C(^3P)$	6.037×10^{-14}	−0.541	33849	Equation (12) of Ref. 1
$C_2(X^1\Sigma_g^+) + O(^3P) \rightarrow CO(D^1\Delta^-) + C(^3P)$	4.163×10^{-13}	−0.541	36262	Equation (12) of Ref. 1
$C_2(d^3\Pi_g) + O(^3P) \rightarrow CO(X^1\Sigma^+) + C(^3P)$	7.662×10^{-12}	−1.259	−14466	Rate coefficient[55]
$O_2(X^3\Sigma_g^-) + C(^3P) \rightarrow CO(a^3\Pi) + O(^3P)$	9.606×10^{-17}	0	348	Rate coefficient[56]
$O_2(X^3\Sigma_g^-) + C(^3P) \rightarrow CO(a'^3\Sigma^+) + O(^3P)$	8.118×10^{-17}	0	1024	Equation (12) of Ref. 1
$O_2(X^3\Sigma_g^-) + C(^3P) \rightarrow CO(d^3\Delta) + O(^3P)$	1.732×10^{-16}	0	1782	Equation (12) of Ref. 1
$O_2(X^3\Sigma_g^-) + C(^3P) \rightarrow CO(e^3\Sigma^-) + O(^3P)$	9.291×10^{-17}	0	1919	Equation (12) of Ref. 1
$O_2(X^3\Sigma_g^-) + C(^3P) \rightarrow CO(D^1\Delta^-) + O(^3P)$	6.314×10^{-18}	0	2127	Equation (12) of Ref. 1

NO have been implemented in CoRaM-MARS. The rate coefficients are due to Chernyi and Losev[59] and to the UMIST database (http://www.udfa.net). The processes involving CN have also been taken into account. The VRP has been used if necessary to derive the vibrational state-dependent rate coefficient. Some rate coefficients given under the modified Arrhenius form $k(T) = A\,T^{\alpha}\,e^{-\Delta E/(k_B T)}$ are given in Table III.

4. Other collisional processes

Additional processes involving carbonated ions and neutrals are now considered like charge exchange, excitation transfer, and reassociation (simultaneous neutral and charge exchange). Some of the required rate coefficients are reported in the UMIST database. The related values range between some 10^{-17} and 10^{-15} m^3 s^{-1} and weakly depend on T_A.

Among the previously mentioned elementary processes, we have considered the dissociative recombination of CO^+, C_2^+, and CN^+. The rate coefficients are taken from the work of Rosén *et al.*[60] and Mezei *et al.*[61] for CO^+, Le Padellec *et al.*[62] for CN^+, and Mitchell[63] for C_2^+. The significance of dissociative recombination has already been put in evidence behind shock fronts.[64] In addition, some excitation transfer processes between CO, NO, and N_2 have been implemented in the model. The rate coefficients are due to Gorelov *et al.*[38]

The excited states of the molecular species can be dissociated under electron impact. We have used Eq. (8) of our paper devoted to air[1] to give the rate coefficient under the form of a modified Arrhenius law for the dissociation involving carbonated species.

All the collisional backward processes derived from the forward processes described above are finally included in the model. Each rate coefficient is determined using the detailed balance principle.

5. Radiative processes

We have taken into account molecular systems and atomic lines due to carbonated species. Table IV lists these additional data. Escape factors have been implemented.[1] Except spontaneous emission, the model has also been enriched by the implementation of radiative recombination whose significance is obvious at low density. Equation (34) of our paper on air[1] based on the cross section due to Zel'dovich and Raizer[65] has been used. Finally, the C^+ dielectronic recombination,

$$C^+ + e^- \rightarrow C(^1D) + h\nu, \tag{12}$$

is also implemented in the model with the rate coefficient determined by Nussbaumer and Storey.[66]

III. RESULTS

A. Martian entry conditions

During its atmospheric entry and before its final crash, the landing module Schiaparelli has interacted with atmospheric layers having different mixing ratios. Above an altitude of ∼130 km, the N_2 and Ar mixing ratios increase with altitude, while they have the same value as on the ground for lower altitudes.[67] The composition is relatively well known since the Viking probe landing and has been recently confirmed by the Mars Science Laboratory mission.[68] The mole fraction of N_2 is equal to that of Ar at 2%. A residual mole fraction is found for O_2 and CO at values equal to 0.15% and 0.06%, respectively. These traces are due to the atmospheric chemistry induced by the solar irradiation. They are too weak to play a significant role. We have therefore assumed their influence negligible. The retained composition is therefore 96% CO_2, 2% N_2, and 2% Ar.

TABLE IV. Additional molecular systems and atomic lines implemented in CoRaM-MARS with respect to CoRaM-AIR.[1] References where the concerned Einstein coefficients can be found are given.

Species	Transitions	System/lines	References
CO_2	$X^1\Sigma_g^+ v'' - X^1\Sigma_g^+ v'$	Infrared	76
CO	$X^1\Sigma^+ v'' - X^1\Sigma^+ v'$	Infrared	77
	$A^1\Pi - X^1\Sigma^+$	Fourth positive	77
	$B^1\Sigma^+ - X^1\Sigma^+$	Hopfield-Birge	77
	$a'^3\Sigma^+ - a^3\Pi$	Asundi	11
	$d^3\Delta - a^3\Pi$	Triplet	11
	$b^3\Sigma^+ - a^3\Pi$	Third positive	77
	$B^1\Sigma^+ - A^1\Pi$	Angström	11
CO^+	$A^2\Pi - X^2\Sigma^+$	Comet-tail	77
	$B^2\Sigma^+ - X^2\Sigma^+$	First negative	77
	$B^2\Sigma^+ - A^2\Pi$	Baldet-Johnson	77
CN	$A^2\Pi - X^2\Sigma^+$	Red	77
	$B^2\Sigma^+ - X^2\Sigma^+$	Violet	77
	$B^2\Sigma^+ - A^2\Pi$	Le Blanc	77
C_2	$A^1\Pi_u - X^1\Sigma_g^+$	Philips	77
	$D^1\Sigma_u^+ - X^1\Sigma_g^+$	Mulliken	77
	$b^3\Sigma_g^- - a^3\Pi_u$	Ballik-Ramsay	77
	$d^3\Pi_g - a^3\Pi_u$	Swan	77
	$C^1\Pi_g - A^1\Pi_u$	Deslandres-D'Azambuja	77
	$e^3\Pi_g - a^3\Pi_u$	Fox-Herzberg	77
C	$C_j \rightarrow C_{i<j} + h\nu$	1369 Lines	NIST
C^+	$C_j^+ \rightarrow C_{i<j}^+ + h\nu$	11 Lines	NIST

The most critical phase of the entry takes place before the deceleration peak, when the thermal flux between the shock layer and the TPS of the spacecraft is maximum. This peak heating (PH) has been predicted around 70 s after the beginning of the entry phase, at an altitude of $z_0 = 45$ km. The actual flight did not confirm these characteristics since they correspond to the plasma blackout phase. However, we have considered these conditions as respected. The module had a speed of $u_0 = 5300$ m s^{-1} at this altitude. The local thermodynamic conditions have been reevaluated through the Mars Science Laboratory mission[69] with respect to the Viking program results.[70] The pressure, the temperature, and the specific mass at z_0 are $p_0 = 7.6$ Pa, $T_{A0} = 162$ K, and $\rho_0 = 2.45 \times 10^{-4}$ kg m^{-3}, respectively. This corresponds to a mean molar mass of 43.4×10^{-3} kg mol^{-1} compatible with the mixing ratio discussed above. In these flight conditions, the Mach number is $\mathcal{M}_0 = 26.4$.

Since flight data have been obtained under an altitude of $z_0 = 28.2$ km after the blackout phase,[71,72] the second trajectory point considered in our study corresponds to this low altitude (LA) where the thermodynamic conditions are $p_0 = 57$ Pa, $T_{A0} = 192$ K, and $\rho_0 = 1.54 \times 10^{-3}$ kg m^{-3}. The speed was $u_0 = 2550$ m s^{-1}. In these flight conditions, the Mach number is $\mathcal{M}_0 = 11.7$. The complete entry conditions are summarized in Table V.

TABLE V. Entry conditions.

Conditions	Altitude z_0, km	Speed u_0, m s^{-1}	Pressure p_0, Pa	Temperature T_{A0}, K	Mach number $\mathcal{M}_0$
(PH)	45	5300	7.6	162	26.4
(LA)	28.2	2550	57	192	11.7

B. Initial conditions

In the (PH) or (LA) entry conditions, a shock layer is formed around the forward heatshield just behind a shock front having a negligible typical thickness. In a first approximation, the Rankine-Hugoniot discontinuity equations can be assumed across the shock front. Electron temperature is assumed frozen since the flow speed is much lower than the electron speed of sound. As a result, the kinetic temperature $T_A(0)$, the pressure $p(0)$, and the Mach number $\mathcal{M}(0)$ of heavy particles just after the shock front before any chemical activity (at the abscissa $x = 0$ in Secs. III D and III E) are given by

$$T_A(0) = \frac{\left[2 + (\gamma - 1)\mathcal{M}_0^2\right]\left[1 - \gamma + 2\gamma\mathcal{M}_0^2\right]}{(\gamma + 1)^2\mathcal{M}_0^2}\, T_{A0}, \tag{13}$$

$$p(0) = \frac{1 - \gamma + 2\gamma\mathcal{M}_0^2}{1 + \gamma}\, p_0, \tag{14}$$

$$\mathcal{M}(0) = \sqrt{\frac{2 + (\gamma - 1)\mathcal{M}_0^2}{1 - \gamma + 2\gamma\mathcal{M}_0^2}}, \tag{15}$$

where a mean value of $\gamma = 1.3$ is used. This value allows us to match the Mach number sequence along the trajectory given by Tran and Beck.[73] The values of $T_A(0)$, $p(0)$, and $\mathcal{M}(0)$ are then the initial conditions of the system of nonlinear ordinary differential equations presented in Sec. III C.

C. 1D Eulerian code

Since electrons and heavy particles are explicitly considered, the energy balance is applied for each type of particle. We reduce our study to the central streamline where the flow can be considered as one-dimensional along the x-axis in a first approximation. Denoting e_A and e_e the internal energy per unit volume, the related equations are written as

$$\frac{d}{dx}\left(\frac{e_A}{\rho} + \frac{p_A}{\rho} + \frac{\rho_A}{\rho}\frac{u^2}{2}\right) = \frac{Q_{e\to A} - \varepsilon_{SE} - Q_{A,RDR}}{\rho u} \tag{16}$$

for heavy particles and

$$\frac{d}{dx}\left(\frac{e_e}{\rho} + \frac{p_e}{\rho} + \frac{\rho_e}{\rho}\frac{u^2}{2}\right) = \frac{-Q_{e\to A} - \varepsilon_{RDR} + Q_{A,RDR}}{\rho u} \tag{17}$$

for electrons, where p_A and p_e are the pressure and ρ_A and ρ_e the specific mass of the heavies and electrons, respectively, with $\rho = \rho_A + \rho_e$. $Q_{e\to A}$ is the energy given per unit time and per unit volume by electrons to heavies through elastic and inelastic/superelastic processes. The energy lost by unit volume of the flow per unit time through radiation (spontaneous emission) excluding radiative recombination and dielectronic recombination is denoted ε_{SE}. The form taken by the energy balance equations (16) and (17) results from the high speed of the flow denoted u. Additional details may be found in Ref. 40.

Equations (16) and (17) also account for the influence of the radiative recombination,

$$A_k^+ + e^- \to A_i + h\nu, \tag{18}$$

for an atom A and of the dielectronic recombination of type (12). These elementary processes have several influences on the balance equations (16) and (17). Indeed, they lead to the emission of a continuum since the elementary energy conservation is written as

$$E_k + \frac{1}{2}\, m_e\, v_e^2 = E_i + h\nu. \tag{19}$$

As a result, a volumic emission coefficient ε_{RDR} (expressed in W m^{-3}) has to be introduced in (17). This term corresponds to the radiation emitted during the capture of the electron by the ion during the process (18). Moreover, radiative and dielectronic recombinations lead to the decrease in the internal energy of the heavy particles since the recombination takes place. The energy $E_k - E_i$ is therefore lost. The related term is denoted $Q_{A,RDR}$ per unit volume per unit time and is introduced in the energy balance for heavies (16). Since the energy conservation equation of the flow is

$$\frac{d}{dx}\left(\frac{e_A + e_e}{\rho} + \frac{p_A + p_e}{\rho} + \frac{u^2}{2}\right) = \frac{-\varepsilon_{SE} - \varepsilon_{RDR}}{\rho u}, \tag{20}$$

an additional term is required in Eq. (17) involving $Q_{A,RDR}$. This term can be considered as the influence of the redistribution of the thermal energy among fewer electrons when the recombination (12) or (18) takes place.

Previous Eqs. (16) and (17) are solved in coupling with the mass conservation

$$\frac{d}{dx}(\rho u) = 0, \tag{21}$$

the momentum conservation

$$\frac{d}{dx}\left(p + \rho u^2\right) = 0, \tag{22}$$

and the balance equation relative to the species X in a vibrational or electronic state i,

$$\frac{dy_{X_i}}{dx} = \frac{m_{X_i}\,[X_{i,CR}]}{\rho u}, \tag{23}$$

using the DVODE library.[74] In Eqs. (22) and (23), $p = p_A + p_e$ is the total pressure, m_{X_i} is the mass of the species X_i, and $[X_{i,CR}]$ is the number density collisional-radiative source term resulting from the elementary processes discussed above.

D. Analysis of the (PH) conditions: $\mathcal{M}_0 = 26.4$

1. Aerodynamic variables

Figure 3 illustrates the aerodynamic variable distribution behind the shock front. Even if the thickness of the shock layer is only of the order of several centimeters, the distribution displayed on this figure is calculated until a quasiuniform zone corresponds to ∼10 m. We can

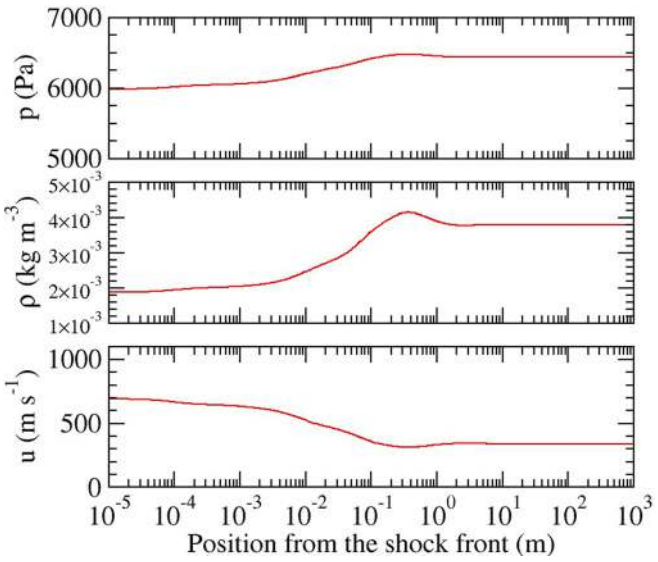

FIG. 3. Evolution behind the shock front (located at $x = 0$) of the aerodynamic variables, pressure p, mass density ρ, and speed u of the flow in the (PH) conditions.

see that the pressure, the mass density, and the speed reach just behind the shock front (located at $x = 0$) values very close to those observed in this area. This means that chemistry induced by the heavy particle temperature T_A behind the shock (close to 17 000 K) has a rather low influence on the aerodynamic variables. We can nevertheless observe this influence for $x \sim 10^{-2}$–10 m where pressure and mass density are increasing, whereas speed is decreasing.

2. Main characteristics of the chemistry

This chemistry is clearly at work in Fig. 4. Indeed, the dissociation of the flow becomes significant at $x \sim 10^{-2}$ m. The density of CO and O increase as well as the one of N. This dissociation phase induces the formation of molecules not present in the incoming flow such as NO and molecular ions, a part of which is subsequently partially dissociated. This dissociation phase also leads to the formation of atomic ions particularly C^+ whose density equilibrates more or less the electron density. The following relaxation enables the formation of NO^+ and CO^+, leading to the electroneutrality of the flow with electrons. The temperature reached in this region is too weak to induce a significant ionization of Ar, whose influence could be neglected in a first approximation.

3. Vibrational distributions and vibrational temperatures

Except Ar^+, CO_2 is the slower species. In the present conditions, its relaxation requires ∼30 m. This behavior is mainly due to the vibrational structure of this molecule. With its second (bending) mode whose states close to the dissociation limit are highly degenerated, the excited states behave like a reservoir when they are sufficiently populated. For $x > 10^{-1}$ m, they are indeed highly populated. But temperatures have significantly decreased, which still leads to the dissociation with lower rates. The dissociation is therefore slowed down but goes on anyway until the final steady state.

An illustration of this reservoirlike behavior is obvious in Figs. 5–7. These figures correspond to the Boltzmann plots of modes 1, 2, and 3, respectively. We see, in particular, in Fig. 6, for mode 2, the strong increase in the ratio between density and degeneracy for $x \sim 10^{-1}$ m. At the same location, this ratio for the mode 2 excited states close to the dissociation limit is higher than those of the other modes by a factor at least equal to 10. Since the degeneracy of these states is $(v_2 + 1)$ and since $v_{2,max} = 66$, the population density is at least higher by a factor of 100. We can therefore assert that the CO_2 molecules in the flow mostly belong to the second (bending) mode.

These figures also illustrate the regime change for the distribution at $x \sim 10^{-3}$ m. This location corresponds to a coupling from the excitation point of view between the states close to the ground state and

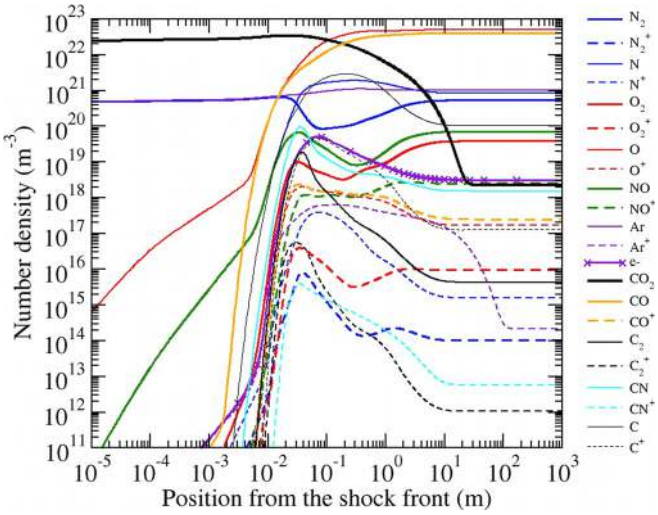

FIG. 4. Evolution behind the shock front of the density of the species in the (PH) conditions (neutrals in continuous lines and charged species in dashed lines).

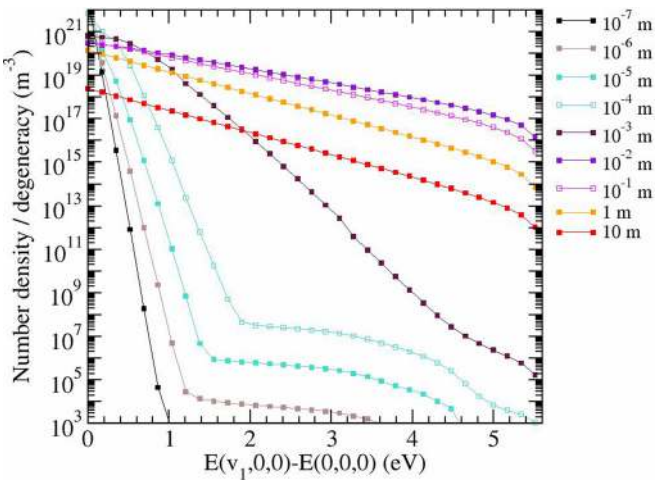

FIG. 5. Boltzmann plot of the CO_2 (v_1, 0, 0) states at $x = 10^{-7}$,...,10 m in the (PH) conditions.

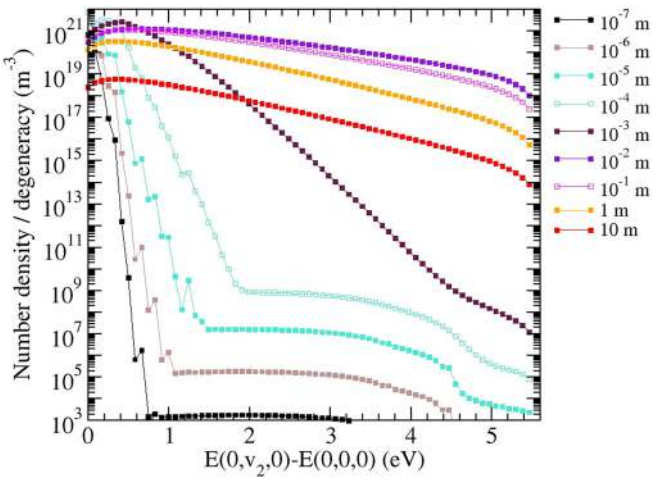

FIG. 6. Boltzmann plot of the CO_2 (0, v_2, 0) states at $x = 10^{-7},\ldots,10$ m in the (PH) conditions.

those close to the dissociation limit. Systematically, the high-lying levels reach rapidly a relatively high excitation temperature characterized by a weakly negative slope of the mean square line interpolating the distribution. The relaxation time of the weakly excited levels is higher, and they remain weakly excited until $x \sim 10^{-3}$ m where the connection between the two distributions takes place. It is also interesting to note that stretching modes reach a quasiequilibrium distribution characterized by linear Boltzmann plots over its most part, whereas the bending mode departs from linear distribution on longer times.

Three types of vibrational temperatures can be postprocessed from the previous distribution to estimate the relevance of this concept. The vibrational temperature $T_{vib,inf}(CO_2)_i$ corresponds to the excitation temperature calculated from the first six vibrational excited states of mode i such as

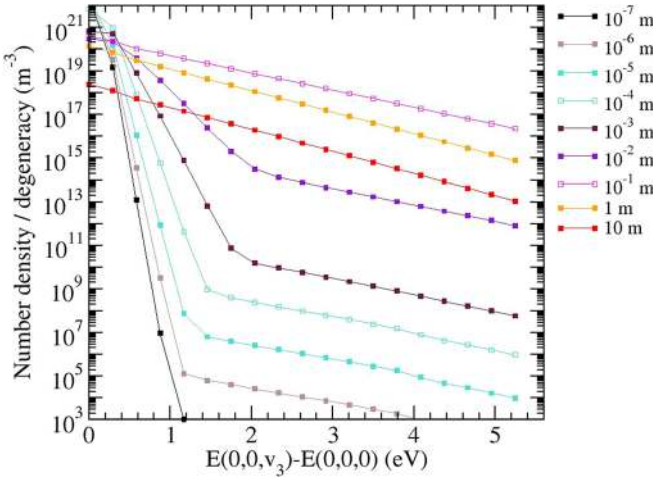

FIG. 7. Boltzmann plot of the CO_2 (0, 0, v_3) states at $x = 10^{-7},\ldots,10$ m in the (PH) conditions.

$$T_v^l(CO_2)_i = -\frac{1}{k_B\left[\frac{d}{dE(v)}\left(\ln\left[CO_2(i,v)\right]\right)\right]_{lsl,0\le v\le 5}}. \quad (24)$$

The vibrational temperature $T_{vib,sup}(CO_2)_i$ corresponds to the excitation temperature calculated from the last six vibrational excited states of mode i such as

$$T_v^u(CO_2)_i = -\frac{1}{k_B\left[\frac{d}{dE(v)}\left(\ln\left[CO_2(i,v)\right]\right)\right]_{lsl,v_{max}-5\le v\le v_{max}}}. \quad (25)$$

The vibrational temperature $T_v^E(CO_2)_i$ corresponds to the equilibrium distribution temperature required to obtain the vibrational energy density for mode i,

$$\sum_v [CO_2(i,v)]\,E(i,v) = \frac{\sum_v [CO_2(i,v)]\ \sum_v g(i,v)\,E(i,v)\,e^{-\frac{E(i,v)}{k_B T_v^E(CO_2)_i}}}{\sum_v g(i,v)\,e^{-\frac{E(i,v)}{k_B T_v^E(CO_2)_i}}}. \quad (26)$$

This definition corresponds to the classical definition of the vibrational temperature. Figures 8–10 display the evolution in space of these different temperatures for the symmetric stretching, the bending, and the asymmetric stretching modes of CO_2, respectively. Electron temperature T_e and heavy particle temperature T_A are also displayed for comparison. We can see that the symmetric stretching and bending modes are satisfactorily coupled to each other, even if some discrepancies can be observed. This is mainly due to the Fermi resonance process (1) that easily promotes the excitation transfer between the modes considered. The vibrational temperatures $T_v^l(CO_2)_i$ and $T_v^E(CO_2)_i$ for modes $i = 1$ and 2 present the same behavior. Starting from T_{A0}, a maximum of around 11 000 K is observed for $x \sim 10^{-2}$ m. Then, a

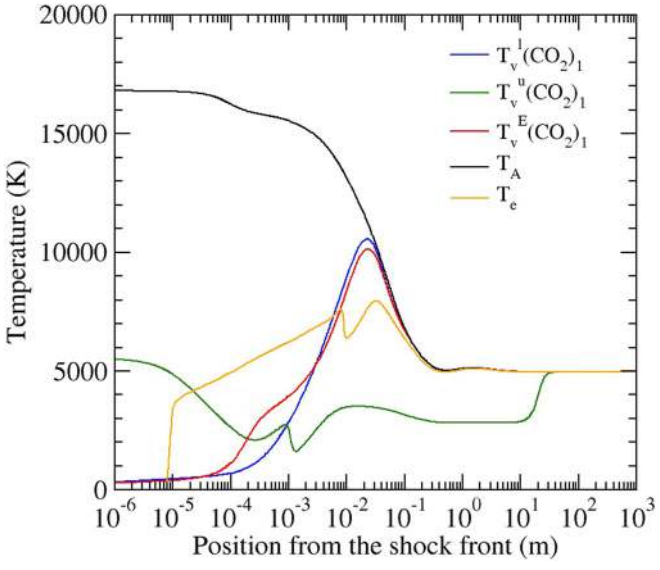

FIG. 8. Distribution of the vibrational temperatures for the symmetric stretching mode of CO_2. T_A refers to the heavy particle temperature and T_e to the electron temperature.

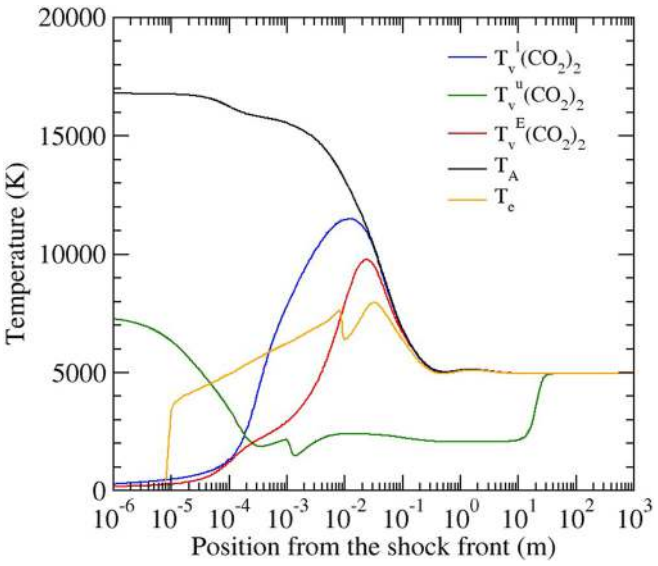

FIG. 9. Distribution of the vibrational temperatures for the bending mode of CO_2. T_A refers to the heavy particle temperature and T_e to the electron temperature.

coupling with T_A and T_e occurs for $x \sim 10^{-1}$ m until the relaxation at ~5000 K for $x > 1$ m. The vibrational temperature $T_v^u(CO_2)_i$ increases rapidly as already seen in Figs. 5–7. They are of the order of 6000 K for $x \sim 10^{-6}$ m. Then, $T_v^u(CO_2)_3$ remains uniform, whereas $T_v^u(CO_2)_i$ decreases abruptly for $i = 1$ and 2. The third (asymmetric stretching) mode also behaves differently from the extremum point of view. The value obtained at $x \sim 10^{-2}$ m is quite lower than the ones obtained for modes 1 and 2. Globally, the third mode is difficult to excite. This is the direct result of the characteristic energy of excitation higher than that for the other vibrational modes.

In the case of the experimental study of similar flows, for instance, produced in shock tubes, the vibrational energy is often considered as characterized by a vibrational temperature defined as the excitation temperature of the vibrational excited states close to the ground. Figures 8–10 clearly show that this assumption is not necessarily obvious in the first centimeter downstream the shock front.

Moreover, Fig. 11 illustrates the comparison between the vibrational temperature defined by Eq. (26) for each mode and the global vibrational temperature $T_v^E(CO_2)$ defined by extending the summation of Eq. (26) to the three modes. This comparison clearly shows that the second (bending) mode drives the global vibrational temperature of CO_2. Indeed, $T_v^E(CO_2)_2$ perfectly matches $T_v^E(CO_2)$. This is due to the degeneracy of the bending mode which results from the ability of the molecule vibrationally excited in this mode to rotate. As already mentioned, the degeneracy of each vibrational level characterized by quantum number v_2 is then $v_2 + 1$. The ability to store numerous molecules in these states is quite high and the influence of $g(2, v)$ in the summations of Eq. (26) is significant. The energy is stored by difficulty in the third (asymmetric stretching) mode. The relaxation times are higher than those for the other modes. But this has no significant influence.

Heavy particle kinetic temperature T_A decreases from the value of $T_A(0) \sim 17\,000$ K resulting from the shock crossing to lower values of the order of 7000 K at $x \sim 10^{-1}$ m. This is due to the energy pumping induced by the vibrational elementary processes. Electron temperature T_e starts from T_{A0} and increases mainly through the (Ve) processes and elastic collisions. The energy stored in translation is then mainly responsible for the vibrational excitation of the other molecules.

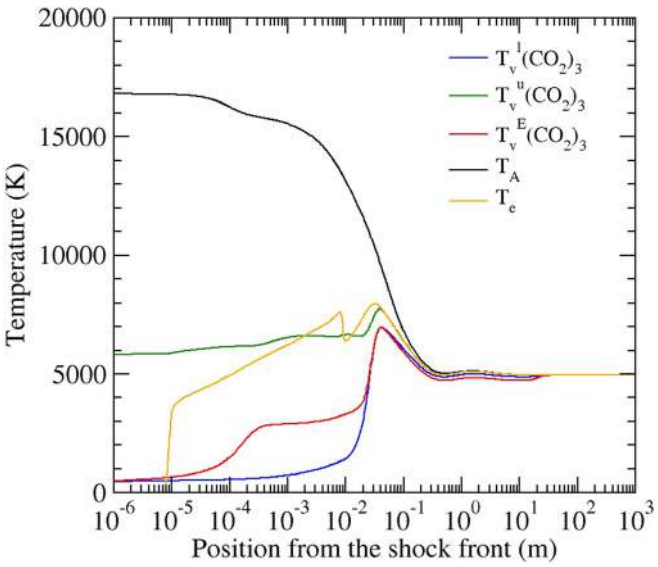

FIG. 10. Distribution of the vibrational temperatures for the asymmetric stretching mode of CO_2. T_A refers to the heavy particle temperature and T_e to the electron temperature.

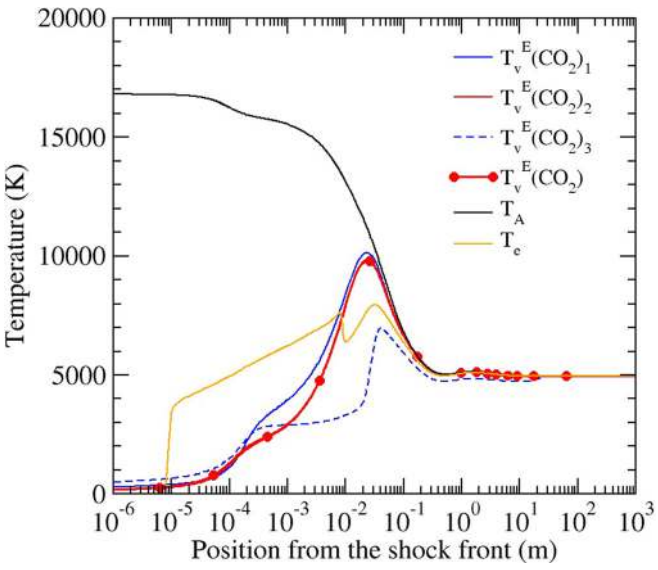

FIG. 11. Distribution of $T_v^E(CO_2)_i$, the energy-defined vibrational temperatures for the different modes i of CO_2, and $T_v^E(CO_2)$, the global vibrational temperature of CO_2. T_A refers to the heavy particle temperature and T_e to the electron temperature.

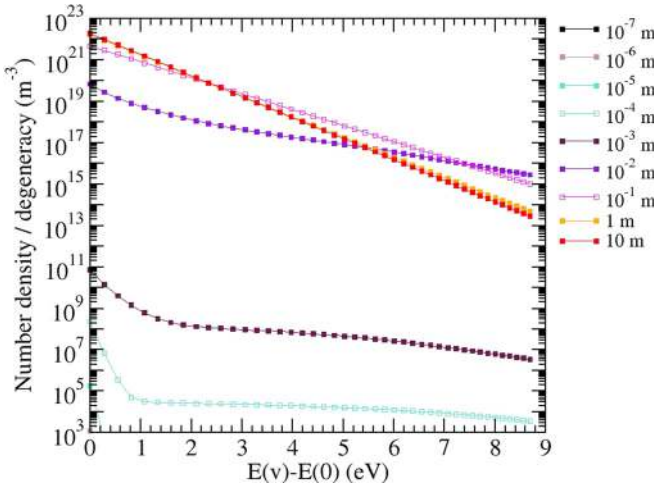

FIG. 12. The same as Fig. 5, but for CO.

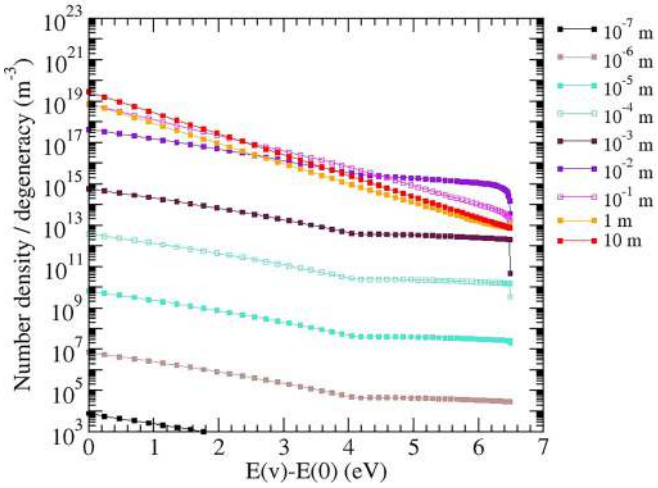

FIG. 13. The same as Fig. 12, but for NO.

Due to the high number of molecules considered in the mixture, we will present the evolution in space of the vibrational distribution for two representative molecular species. The first one is CO whose formation is promoted by the dissociation of CO_2. Figure 12 illustrates the evolution of Boltzmann plots with x. Similar to CO_2, the distribution is characterized by a low vibrational energy part whose excitation temperature is lower than that for the high vibrational energy part. Nevertheless, in the present case, the coupling between the two parts is more rapid than in the case of CO_2. This is mainly due to the fact that CO does not exist upstream the shock front. The vibrational ground state is therefore very weakly populated just past the shock front. We can also see similar to Figs. 5–7 that the distribution exhibits a plateau close to the shock front ($x < 10^{-4}$ m). This behavior is due to heavy particle induced collisions. In this part of the flow, heavy particle temperature and density are sufficiently high to induce such a coupling.

Figure 13 displays the results obtained for NO. Since this molecule is not present in the flow crossing the shock front, NO is produced through the Zel'dovich elementary processes,

$$N_2(v) + O \rightarrow NO(v') + N, \tag{27}$$

directly at high vibrational excitation due to the (VRP). We had already observed such a behavior with CoRaM-AIR.[1] The difference in terms of excitation between the weakly excited vibrational states and the highly excited vibrational states is lower than that in the previous cases. Moreover, the coupling with the dissociation continuum is difficult as illustrated by the density of the last vibrational state. Indeed, at $x \sim 10^{-4}$–10^{-3} m, we can see that the underpopulation of this state is significant with respect to the other states close to the dissociation limit. At this location, the dissociation is due to the molecular impact since the dissociation degree is very small. The last vibrational state is therefore only involved in the process, which leads to a strong discrepancy of the related number density with respect to the others. When the dissociation degree has sufficiently increased to enable the dissociation through atomic impact, the distribution is smoothed since all the excited vibrational states are concerned. The smoothing is reinforced by the VT processes and finally leads to a linear distribution.

4. Molecular excited states

Triplet states have been considered, but the related densities remain rather weak and do not participate fundamentally in the chemistry.

CO is the most important molecule in the flow in terms of density. We therefore present in Fig. 14 its density field including the first ten vibrational excited states of the X electronic state, as well as the one of CO^+. We can see that the excited electronic states do not contribute significantly to the total carbon monoxide density. Except the $D^1\Delta^-$, $b^3\Sigma^+$, and $B^1\Sigma^+$ states, the dissociation following the excitation phase around $x \sim 10^{-2}$ m leads to a decrease of two orders of magnitude in the population density of the states. This means that the radiative signature due to the systems listed in Table IV is mainly observed for $x \sim 10^{-2}$ m. The figure also displays the distribution of the CO^+ population density whose values remain rather weak.

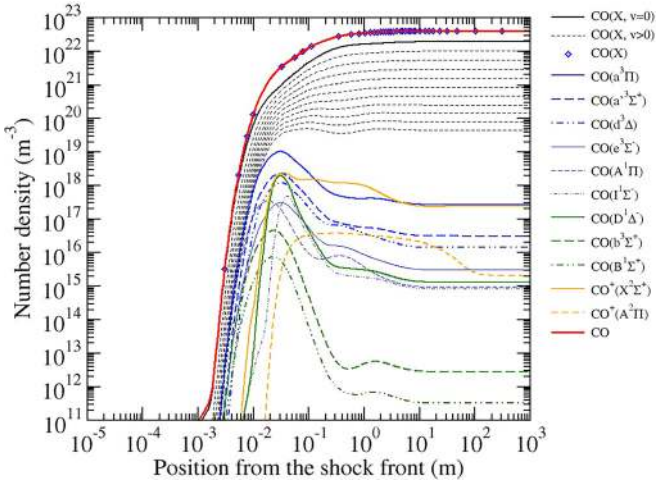

FIG. 14. The same as Fig. 4, but for the electronic states of CO and CO^+.

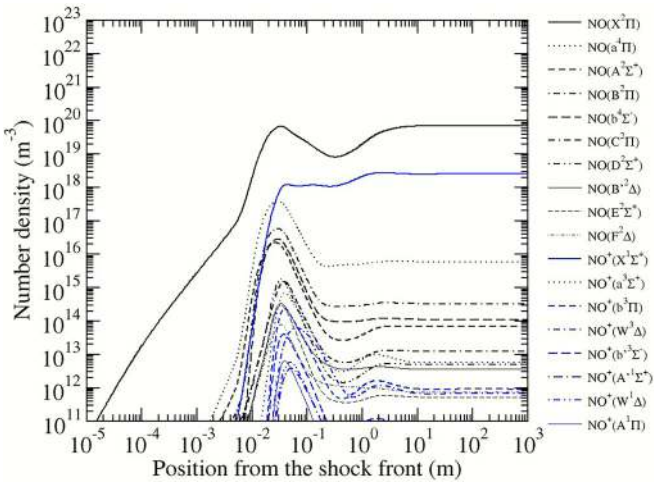

FIG. 15. The same as Fig. 4, but for the electronic states of NO and NO^+.

For $x < 1$ m, the main ionic species is C^+ and is replaced by NO^+ at a higher distance from the shock front. We consequently present in Fig. 15 the distribution of the population density of NO^+ as well as those of NO. In the two cases, the excited states are weakly populated. This results mainly from the temperature in the region $x > 1$ m whose value does not exceed 5000 K.

E. Analysis of the (LA) conditions: $\mathcal{M}_0 = 11.7$

To obtain information on the flow in the conditions of the data collected after the blackout phase, we have chosen to consider the (LA) flight conditions (see Table V). Figure 16 illustrates in these conditions the distribution of the species in the flow from the shock front. We can see that the dissociation degree is very weak. Indeed, at $x = 0.1$ m, its value is $\sim 10^{-6}$. This is mainly due to the temperature and the pressure behind the shock front whose values are close to 4000 K and 9000 Pa, respectively. No ion type can be significantly produced in such conditions. The weak temperature level extends the time scales over which the main processes take place. As a result, a no physical position of ~100 m from the shock front is necessary to obtain a significant dissociation degree. Figure 17 displays the distribution of the kinetic temperature T_A within the flow. After the shock front at a value close to 4000 K, T_A decreases until ~3000 K for $x > 4 \times 10^{-3}$ m due to the vibrational pumping.

In this figure is also displayed the distribution of the vibrational temperature of the CO_2 modes. We can see that the first and the second vibrational modes remain coupled as in the case of the (PH) conditions. The coupling is perhaps better since the difference between $T_v^l(CO_2)$ and $T_v^E(CO_2)$ is lower for each mode. The discrepancies observed with mode 3 are higher in the present case than for the (PH) conditions. Indeed, the evolution is delayed by three orders of magnitude with a final coupling observed at $x \sim 10^1$ m, whereas the coupling between modes 1 and 2 is obvious at $x \sim 10^{-2}$ m.

This figure illustrates the distribution of the vibrational temperature of the ground state of NO, N_2, and CO in terms of vibrational energy storage defined by Eq. (26). Figure 13 shows that NO is produced with a high vibrational temperature in the (PH) conditions since the Boltzmann plots around the ground vibrational state have a negative slope close to 0. NO is therefore directly produced in excited vibrational states. This excitation of the products results from the (VRP) and from the main channel of production of NO by neutral (Zel'dovich) exchange $N_2 + O \rightarrow NO + N$. In the present (LA) conditions, NO is still produced with a high vibrational excitation and the vibrational temperature calculated using Eq. (26) is close to 10 000 K before the complete coupling for $x > 10^1$ m at ~3000 K. For N_2, the distribution of the vibrational temperature illustrates the quasiresonance of ω_e between N_2 and the third mode of CO_2. Since the vibrational excitation of N_2 is weak, the coupling is obtained with $T_v^l(CO_2)_3$ and not with $T_v^E(CO_2)_3$. Finally, the vibrational excitation of CO is intermediate as a result of the influence of the different elementary processes.

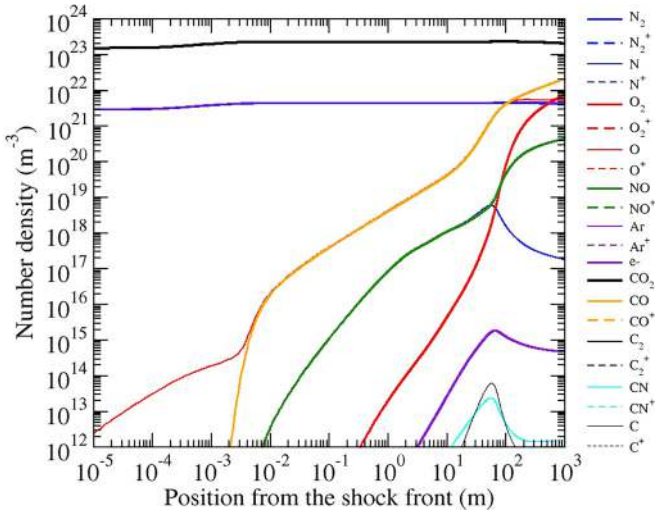

FIG. 16. Evolution behind the shock front of the density of the species in the (LA) conditions (neutrals in continuous lines and charged species in dashed lines).

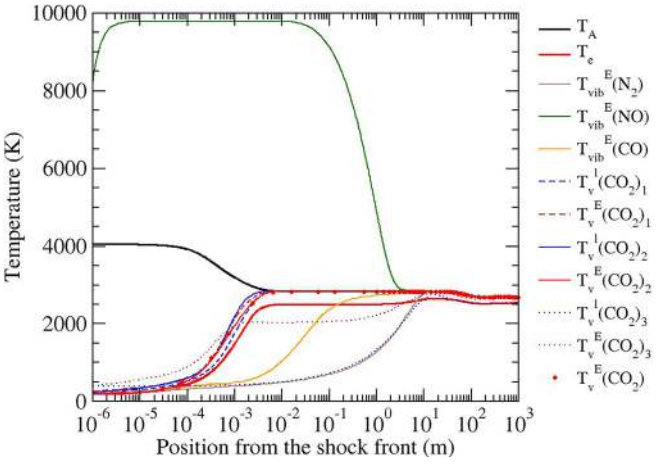

FIG. 17. Evolution behind the shock front of different characteristic temperatures in the (LA) conditions.

The final coupling is more or less obtained at locations very far from the shock front. Of course, since the shock layer has a thickness of several centimeters, it is obvious that this coupling will not be obtained. The edge of the boundary layer will be therefore out of thermochemical equilibrium.

F. Relative role of electrons and heavies in the collisional processes

Due to their different efficiency in terms of collisions and to the thermal nonequilibrium in the flow, electrons and heavy particles have been separately considered in the present model. For the (LA) conditions studied in Sec. III E, electrons clearly do not play a significant role. Indeed, electron density and temperature are too weak to have any influence on the chemistry. Conversely, for the (PH) conditions, the role played by electrons is clearly stronger. However, their density and temperature have to be high enough. Since electron density is 0 upstream, the vibrational excitation and therefore the dissociation degree are mainly driven by the heavy particles in the first centimeters of the flow. For positions farther from the shock front, whereas the vibrational excitation is already significant, electrons have reached high temperature and density. Then, they act on the vibrational distributions.

IV. CONCLUSION

In this paper, we have reported the elaboration and the implementation in a 1D Eulerian CFD code of the collisional-radiative model CoRaM-MARS especially developed for Martian entries. This model takes into account CO_2, N_2, and Ar as well as all the species possibly produced when chemistry takes place. The model is vibrationally and electronically specific with 445 vibrational states (electronic ground states of neutral molecules only and vibrational excitation of CO_2 considered in its three modes without preferential coupling) and 1139 electronic states, respectively. A complete set of forward and backward elementary processes is considered involving excitation vibrational processes, dissociation, electronic excitation, ionization, neutral and charge exchanges, excitation transfer, reassociation, dissociative recombination, dielectronic and radiative recombination, and spontaneous emission.

In relation to the EXOMARS mission of 2016 and for the analysis of the flight of the Schiaparelli module, we have studied the postshock flow induced by the atmospheric entry for two Mach number conditions. The first situation corresponds to the peak heating at the surface of the thermal protection system of the module. The second situation corresponds to conditions just after the blackout phase for which measurements by different sensors have been performed and are currently under analysis. We have particularly focused our attention on the first situation because it enables the formation of the greater part of the species involved in the model. All calculations have been performed assuming a discontinuity at the shock front location driven by the Rankine-Hugoniot equations.

For the first situation, the flow is in thermochemical nonequilibrium over some centimeters. For CO_2, the second (bending) mode is the most efficient from the energy storage point of view. The Fermi resonance ensures a very good coupling between this mode and the first (symmetric stretching) mode without a significant difference in terms of vibrational temperature. Even if the triplet states of CO_2 have been considered, they do not play a significant role. The electron density reaches rapidly significant values to play a role in the chemistry. The dissociation degree is also significant with O as major atomic species. For NO and O_2 whose formation is mainly due to neutral exchange mechanisms, the vibrational excitation is strong very close to the shock front.

About the second situation at a lower Mach number, the dissociation degree remains very weak even far from the shock front. Except for this lower dissociation degree and the lower excitation resulting from the lower value of the specific energy, the conclusions previously highlighted above at a high Mach number are globally similar. All these results will support the interpretation of the measurements performed using the different sensors embedded aboard the module.

ACKNOWLEDGMENTS

The authors acknowledge the French Spatial Agency "Centre National d'Etudes Spatiales" and the "Région Haute-Normandie" for their financial support. The authors also acknowledge (1) Dr. Vincenzo Laporta for the data related to vibrational excitation and dissociation rate coefficients of $N_2(X, v)$, $O_2(X, v)$, $NO(X, v)$, and $CO(X, v)$ under electron impact and (2) Dr. Philippe Rivière from the EM2C laboratory, CentraleSupelec and Dr. Yacine Babou for the data related to the Einstein coefficients of the radiative systems of CO, C_2, CN, and CO^+. A part of the research leading to these results has received funding from the European Community's 7th Framework Programme (FP7/2007/2013) under Grant Agreement No. 242311.

REFERENCES

[1]J. Annaloro and A. Bultel, Phys. Plasmas **21**, 123512 (2014).
[2]A. L. Brun and P. Omaly, "Investigation of radiative heat fluxes for Exomars entry in the Martian atmosphere," in *ESA Special Publication Vol. 689* (ESA, 2011), p. 22.
[3]S. Tashkun, V. Perevalov, J.-L. Teffo, L. Rothman, and V. tyuterev, J. Quant. Spectrosc. Radiat. Transfer **60**, 785–801 (1998).
[4]J. Annaloro, A. Bultel, and P. Omaly, AIAA Paper No. 2011-3954, 2011.
[5]J. Annaloro, A. Bultel, and P. Omaly, J. Phys.: Conf. Ser. **511**, 012053 (2014).
[6]T. Kozak and A. Bogaerts, Plasma Sources Sci. Technol. **24**, 015024 (2015).
[7]T. Silva, M. Grofulovic, B. Klarenaar, A. Morillo-Candas, O. Guaitella, R. Engeln, C. Pintassilgo, and V. Guerra, Plasma Sources Sci. Technol. **27**, 015019 (2018).
[8]A. Berthelot and A. Bogaerts, Plasma Sources Sci. Technol. **26**, 115002 (2017).
[9]Y. Babou, "Transferts radiatifs dans les plasmas de mélange CO_2-N_2: Base de données spectroscopiques, étude exp érimentale et application aux rentrées atmosphériques," Ph.D. thesis (Laboratoire EM2C, Ecole Centrale Paris, 2007).
[10]K. P. Huber and G. Herzberg, *Molecular Spectra and Molecular Structure* (Van Nostrand Reinhold Company, 1979).
[11]M. L. da Silva, "Simulation des propriétés radiatives du plasma entourant un véhicule traversant une atmosphère planétaire à vitesse hypersonique: Application à la planète Mars," Ph.D. thesis (Laboratoire ICARE, Université d'Orléans, 2004).
[12]P. J. Bruna and J. S. Wright, J. Phys. Chem. **96**, 1630–1640 (1992).
[13]J. P. Maier and M. Rösslein, J. Chem. Phys. **88**, 4614–4620 (1988).
[14]C. Petrongolo, P. J. Bruna, and S. D. Peyerimhoff, J. Chem. Phys. **74**, 4594–4602 (1981).
[15]R. Wang, Z. H. Zhu, and C. L. Yang, J. Mol. Struct. **571**, 133–138 (2001).
[16]K. A. Peterson, J. Chem. Phys. **102**, 262–270 (1995).
[17]R. Polak and J. Fiser, Spectrochim. Acta, Part A **58**, 2029–2041 (2002).
[18]P. H. Krupenie, "The band spectrum of carbon dioxide," Technical Report No. NSRDS-NBS-5 (1966).
[19]K. Okada and S. Iwata, J. Chem. Phys. **112**, 1804–1808 (2000).

[20]L. Pietanza, G. Colonna, G. D'Ammando, A. Larrichiuta, and M. Capitelli, Phys. Plasmas **23**, 013515 (2016).
[21]L. Pietanza, G. Colonna, and M. Capitelli, Plasma Sources Sci. Technol. **27**, 095004 (2018).
[22]D. Bruno, M. Capitelli, F. Esposito, S. Longo, and P. Minelli, Chem. Phys. Lett. **360**, 31–37 (2002).
[23]M. Panesi, R. L. Jaffe, D. Schwenke, and T. E. Magin, J. Chem. Phys. **138**, 044312 (2013).
[24]M. Panesi, A. Munafo, T. E. Magin, and R. L. Jaffe, Phys. Rev. E **90**, 013009 (2014).
[25]V. Joly and A. Roblin, Aerosp. Sci. Technol. **3**, 229–238 (1999).
[26]K. F. Herzfeld, J. Chem. Phys. **47**, 743–752 (1967).
[27]J. A. Blauer and G. R. Nickerson, AIAA Paper No. 74-536, 1974.
[28]R. N. Schwartz, Z. I. Slawsky, and K. F. Herzfeld, J. Chem. Phys. **20**, 1591–1599 (1952).
[29]Y. Itikawa, J. Phys. Chem. Ref. Data **31**, 749–767 (2002).
[30]A. Fridman, *Plasma Chemistry* (Cambridge University Press, 2008).
[31]M. L. da Silva, V. Guerra, and J. Loureiro, J. Thermophys. Heat Transfer **21**, 40–49 (2007).
[32]M. Capitelli, C. Ferreira, B. Gordiets, and A. Osipov, *Plasma Kinetics in Atmospheric Gases* (Springer, 2000).
[33]I. Armenise, M. Capitelli, G. Colonna, and C. Gorse, J. Thermophys. Heat Transfer **10**, 397–405 (1996).
[34]V. Laporta, R. Celiberto, and J. M. Wadehra, Plasma Sources Sci. Technol. **21**, 055018 (2012).
[35]V. Laporta, C. M. Cassidy, J. Tennyson, and R. Celiberto, Plasma Sources Sci. Technol. **21**, 045005 (2012).
[36]V. Laporta, D. Little, R. Celiberto, and J. Tennyson, Plasma Sources Sci. Technol. **23**, 065002 (2014).
[37]C. Park, AIAA Paper No. 2008-1446, 2008.
[38]V. A. Gorelov, M. K. Gladyshev, A. Y. Kireev, V. G. Tchebureev, and S. V. Shilenkov, "Non equilibrium ionization and radiation behind shock wave in Martian atmosphere," in *ESA Special Publication Vol. 426* (ESA, 1998), pp. 429–436.
[39]J. Lecointre, D. S. Belic, H. Cherkani-Hassani, J. J. Jureta, and P. Defrance, J. Phys. B **39**, 3275–3297 (2006).
[40]A. Bultel and J. Annaloro, Plasma Sources Sci. Technol. **22**, 025008 (2013).
[41]O. E. Krivonosova, S. A. Losev, V. P. Nalivayko, Yu. K. Mukoseev, and O. P. Shatalov, Plasma Chem. Energoatomizdat **14**, 3–31 (1987) (in Russian).
[42]J. Annaloro, "Modèles collisionnels-radiatifs appliqués aux situations d'entrée atmosphérique martienne et terrestre," Ph.D. thesis (CORIA, Université de Rouen, 2013).
[43]M. Capitelli, G. Colonna, and F. Esposito, J. Phys. Chem. A **108**, 8930–8934 (2004).
[44]F. Esposito, I. Armenise, G. Capitta, and M. Capitelli, Chem. Phys. **351**, 91–98 (2008).
[45]F. Esposito, I. Armenise, and M. Capitelli, Chem. Phys. **331**, 1–8 (2006).
[46]S. T. Surzhikov, "Electronic excitation in air and carbon dioxide gas," Technical Report No. 162 (DTIC Document, 2009).
[47]G. N. Zalogin, P. V. Kozlov, L. A. Kuznetsova, S. A. Losev, V. N. Makarov, Y. V. Romanenko, and S. T. Surzhikov, Tech. Phys. **46**, 654–661 (2001).
[48]R. Riahi, P. Teulet, N. Jaidane, and A. Gleizes, Eur. Phys. J. D **56**, 67–72 (2010).
[49]R. Olszewski, P. Wolinski, and M. Zubek, Chem. Phys. Lett. **297**, 537–542 (1998).
[50]M. J. Brunger and S. J. Buckman, Phys. Rep. **357**, 215–458 (2002).
[51]C. Park, AIAA Paper No. 2008-1206, 2008.
[52]R. S. Freund, R. C. Wetsel, and R. J. Shul, Phys. Rev. A **41**, 5861–5868 (1990).
[53]H. W. Drawin, Report No. DPh-PFC/SRFC-383 (1966).
[54]J. Annaloro, V. Morel, A. Bultel, and P. Omaly, Phys. Plasmas **19**, 073515 (2012).
[55]A. Aliat, Physica A **387**, 4163–4182 (2008).
[56]G. P. Smith, D. M. Golden, M. Frenklach, N. W. Moriarty, B. Eiteneer, M. Goldenberg, C. T. Bowman, R. K. Hanson, S. Song, W. C. Gardiner, Jr., V. V. Lissianski, and Z. Qin, see http://combustion.berkeley.edu/gri-mech/version30/text30.html version30/text30.html for information about the rate coefficient of the O2-C exchange, 2016.
[57]E. Wigner and E. E. Witmer, Z. Phys. **51**, 859–886 (1928).
[58]A. Collins, D. Dominey, and T. Swan, "Review of the gaseous oxidation of pyrocarbon and of the Boudouard reaction," Technical Report No. 1588 (Central Electricity Generating Board, Berkeley (England), Berkeley Nuclear Labs., 1970).
[59]G. G. Chernyi and S. A. Losev, ISTC Report No. 036-96 (1999).
[60]S. Rosen, P. Peverall, M. Larsson, A. LePadellec, J. Semaniak, A. Larson, C. Stromholm, W. J. van der Zande, H. Danared, and G. H. Dunn, Phys. Rev. A **57**, 4462–4471 (1998).
[61]J. Z. Mezei, R. D. Backodissa-Kiminou, D. E. Tudorache, V. Morel, K. Chakrabarti, O. Motapon, O. Dulieu, J. Robert, W.-U. Tchang-Brillet, A. Bultel, X. Urbain, J. Tennyson, K. Hassouni, and I. F. Schneider, Plasma Sources Sci. Technol. **24**, 035005 (2015).
[62]A. Le Padellec, J. B. A. Mitchell, A. Al-Khalili, H. Danared, A. Kallberg, A. Larson, S. Rosén, M. af Ugglas, L. Viktor, and M. Larsson, J. Chem. Phys. **110**, 890 (1999).
[63]J. B. A. Mitchell, Phys. Rep. **186**, 215–248 (1990).
[64]A. Bultel, J. Annaloro, and M.-C. Druguet, EPJ Web Conf. **84**, 06005 (2015).
[65]Y. B. Zel'dovich and Y. P. Raizer, *Physics of Shock Waves and High-Temperature Hydrodynamic Phenomena* (Dover, Mineola, 2002).
[66]H. Nussbaumer and P. J. Storey, Astron. Astrophys., Suppl. Ser. **56**, 293–312 (1984).
[67]P. Mahaffy, M. Benna, M. Elrod, R. Yelle, S. Bougher, S. Stone, and B. Jakosky, Geophys. Res. Lett. **42**, 8951, https://doi.org/10.1002/2015GL065329 (2015).
[68]P. Mahaffy, C. Webster, S. Atreya, H. Franz, M. Wong, P. Conrad, D. Harpold, J. Jones, L. Leshin, H. Manning, T. Owen, R. Pepin, S. Squyres, M. Trainer, and MSL Science Team, Science **341**, 263 (2013).
[69]C. Holstein-Rathlou, A. Maue, and P. Withers, Planet. Space Sci. **120**, 15–23 (2016).
[70]A. Seiff and D. Kirk, J. Geophys. Res. **82**, 4364–4378, https://doi.org/10.1029/JS082i028p04364 (1977).
[71]A. Gulhan, T. Thiele, F. Siebe, R. Kronen, and T. Schleutker, J. Spacecr. Rockets **56**, 68–81 (2019).
[72]A. Gulhan, T. Thiele, F. Siebe, and R. Kronen, Space Sci. Rev. **214**, 12 (2018).
[73]P. Tran and J. Beck, "Exomars entry demonstrator module aerodynamics," in *ESA Special Publication Vol. 692* (ESA, 2011), pp. 3.1–3.10
[74]P. N. Brown, G. D. Byrne, and A. C. Hindmarsh, "VODE: A variable-coefficient ODE solver," SIAM J. Sci. Stat. Comput. **10**, 1038–1051 (1989).
[75]A. Chiroux de Gavelle de Roany, C. Flament, J. W. Rich, and V. V. Subramaniam, AIAA J. **31**, 119–128 (1993).
[76]L. Rothman, I. Gordon, R. Barber, H. Dothe, R. Gamache, A. Goldman, V. Perevalov, S. Tashkun, and J. Tennyson, J. Quant. Spectrosc. Radiat. Transfer **111**, 2139–2150 (2010).
[77]Y. Babou, P. Rivière, M.-Y. Perrin, and A. Soufiani, J. Quant. Spectrosc. Radiat. Transfer **110**, 89–108 (2009).